ADVANCED FUNCTIONAL MATERIALS
www.afm-journal.de

Emerging Dual-Channel Transition-Metal-Oxide Quasiaerogels by Self-Embedded Templating

Hele Guo, Jun Zhou, Qianqian Li, Yueming Li, Wei Zong, Jixin Zhu, Jingsan Xu, Chao Zhang, and Tianxi Liu**

The lack of precise control of particle sizes is the critical challenge in the assembly of 3D interconnected transition-metal oxide (TMO) for newly-emerging energy conversion devices. A self-embedded templating strategy for preparing the TMO@carbon quasiaerogels (TMO@C-QAs) is proposed. By mimicking an aerogel structure at a microscale, the TMO@C-QA successfully assembles size-controllable TMO nanoparticles into 3D interconnected structure with surface-enriched carbon species. The morphological evolutions of intermediates verify that the self-embedded Ostwald ripening templating approach is responsible for the dual-channel TMO@C-QA formation. The general self-embedded templating strategy is easily extended to prepare various TMO@C-QAs, including the Co_3O_4@C-QA, Mn_3O_4@C-QA, Fe_2O_3@C-QA, and NiO@C-QA. Benefiting from the unparalleled 3D interconnected network of aerogels, the Co_3O_4@C-QA displays superior bifunctional catalytic activities for oxygen evolution reaction (OER) and hydrogen evolution reaction (HER), as well as high specific capacity and excellent long-term stability for lithium-ion battery (LIB) anode. A proof-of-concept battery-powered electrolyzer with Co_3O_4@C-QA cathode and anode powered by a full LIB with Co_3O_4@C-QA anode is presented. The battery-powered electrolyzer made of the state-of-the-art TMOs can exhibit great competitive advantages due to its supreme multifunctional energy conversion performance for future water electrolysis.

1. Introduction

Transition-metal oxide (TMO) has recently attracted tremendous attention for the application to crucial electrochemical reactions, i.e., the oxygen evolution reaction (OER) and hydrogen evolution reaction (HER) and lithium-ion battery (LIB) anode.[1–5] TMO nanoparticles with large surface area and fully exposed active sites usually exhibit highly efficient electrochemical activities compared to the bulk state.[6–11] However, the inevitable agglomeration of the TMO nanoparticles, triggered by their unstable thermodynamic parameters, will cause a significant reduction in an accessible active area and subsequent degradation of electrochemical performance.[12,13] The assembly of TMO nanoparticles into a 3D interconnected network structure provides a universally applicable approach to solving the outlined challenge. First, 3D assembly of TMO nanoparticles effectively inhibits their intrinsic agglomeration, thus, maintaining the large surface area and fully exposed active sites.[14] Second, the abundant interconnected pores in 3D structure provides highly efficient ion migration channels.[15–17] Third, 3D assembly of TMO nanoparticles significantly improves the structural integrity by releasing internal stress in all directions.[5,18] However, the preparation methods and the template selections hinder the well interconnected 3D network construction of TMO nanoparticles.[11,19,20]

Aerogel, a 3D interconnected solid network structure with more than 90% occupied air, is a new classification of porous

H. Guo, J. Zhou, Q. Li, Y. Li, W. Zong, Prof. C. Zhang, Prof. T. X. Liu
State Key Laboratory for Modification of Chemical Fibers and Polymer Materials
College of Materials Science and Engineering
Donghua University
Shanghai 201620, P. R. China
E-mail: czhang@dhu.edu.cn; txliu@fudan.edu.cn

H. Guo, Prof. T. X. Liu
Key Laboratory of Synthetic and Biological Colloids
Ministry of Education
School of Chemical and Material Engineering
Jiangnan University
Wuxi 214122, P. R. China

The ORCID identification number(s) for the author(s) of this article can be found under https://doi.org/10.1002/adfm.202000024.

Prof. J. Zhu
Shaanxi Institute of Flexible Electronics (SIFE)
Northwestern Polytechnical University (NPU)
127 West Youyi Road, Xi'an 710072, P. R. China

Dr. J. Xu
School of Chemistry
Physics and Mechanical Engineering
Queensland University of Technology
Brisbane, QLD 4001, Australia

Prof. T. X. Liu
Key Laboratory of Materials Processing and Mold (Zhengzhou University)
Ministry of Education
Zhengzhou 450002, P. R. China

DOI: 10.1002/adfm.202000024

materials with high surface area and nanoscale pore sizes.[21–24] Since Kistler pioneered the first generation of SiO_2 aerogels,[25] numerous aerogels have been developed including inorganic, organic, inorganic/organic hybrid and carbon aerogels.[26–29] The 3D interconnected aerogel structure design provides an efficient approach for preparing metal oxides with prominent properties. Currently, the main-group metal oxide aerogels (i.e., SiO_2, ZrO_2, $A1_2O_3$, Ga_2O_3), are typically prepared through the sol–gel transition from metal alkoxides precursors and subsequent supercritical drying.[30–33] However, the metal alkoxides are usually toxic and expensive, and the overall fabrication process is high energy-consuming.[34] More importantly, low-valence state transition-metal alkoxides (e.g., Co, Ni, Mn) have poor stability and fast hydrolysis rate, inevitably resulting in the collapse of the pore structure and uncontrollable particle size of as-prepared TMO aerogels. Therefore, developing a general preparation method of TMO aerogel with controllable particle size and porosity remains a significant challenge.[35–37]

Here, a self-embedded templating strategy is proposed for preparing TMO@carbon quasiaerogels (TMO@C-QAs). This method assembles Co_3O_4 nanoparticles with surface-enriched carbon species assembly into a 3D interconnected network by mimicking the unique structure of aerogels at the microscale. The accurate morphology evolution of intermediates in different reaction stages confirm that self-embedded templating process of TMO@C-QA takes place via Ostwald ripening templating mechanism. Due to the formation of the dual-channel structure of electrochemical active TMO with tunable sizes and surface-enriched carbon species, the as-obtained TMO@C-QA shows large surface areas, fully exposed active sites and reduced electrical resistance between individual TMO nanoparticles. The self-embedded templating strategy is applicable to preparing a variety of TMO@C-QA, including Co_3O_4@C-QA, Fe_2O_3@C-QA, NiO@C-QA, and Mn_3O_4@C-QA. Taking the Co_3O_4@C-QA as an example, the Co_3O_4@C-QA with the unique quasiaerogel structure exhibits a superior OER and HER bifunctional electrocatalytic activity, as well as excellent electrochemical energy storage performance for LIB anode. A proof-of-concept battery-powered water electrolysis device employing the Co_3O_4@C-QA as HER/OER bifunctional electrocatalysts is demonstrated, powered by the full LIB with the Co_3O_4@C-QA as anode.

2. Results and Discussion

Figure 1 illustrates the preparation procedure of the Co_3O_4@C-QA, mainly involving three steps. First, carbogels were prepared via hydrothermal carbonization using glucose and borax as the precursor and structure-directing agent, respectively. The carbogel-1, carbogel-2, carbogel-3, and carbogel-4 represent the carbogels with the glucose/borax weight ratio of 240, 60, 24, and 10, respectively. Field-emission scanning electron microscopy (FESEM) images of the carbogels show a 3D interconnected aerogel structure consisting of carbon nanoparticle subunits with a narrow particle size distribution (Figure S1, Supporting Information). The diameter of carbon nanoparticle subunits significantly decreases with a decreased glucose/borax ratio, because borax will accelerate the polycondensation/carbonization rate by increasing the number of nucleation seeds during hydrothermal carbonization.[38] Figure S2a (Supporting Information) shows the X-ray photoelectron spectroscopy (XPS) spectra of the carbogel-3, and only the C 1s and O 1s peaks are observed. There is almost no signal of boron species within the carbogel-3, since the water washing easily removes them during the preparation and purification of the carbogels (Figure S2b, Supporting Information). Next, Co ion-infiltrated carbogels (Co-carbogels) were prepared by a penetration-solidification strategy, and the Co-carbogels display a similar morphology to carbogel precursors (Figure S3, Supporting Information). The stretching vibration of −OH in Fourier transform infrared (FTIR) spectrum of Co-carbogels red-shifts from 3450 to 3430 cm^{-1} compared with that of carbogels (Figure S4, Supporting Information), suggesting the efficient adsorption of Co ions on the carbogels.[39] Consequently, during the combustion process in the air at a high temperature, the Co_3O_4@C-QA-1, Co_3O_4@C-QA-2, Co_3O_4@C-QA-3, and Co_3O_4@C-QA-4 can duplicate the 3D interconnected aerogel structure of the carbogel-1, carbogel-2, carbogel-3, and carbogel-4, respectively. The X-ray diffraction (XRD) patterns of the Co-carbogel treated at different temperatures have been measured and presented in Figure S5 (Supporting Information). The Co species do not transform into Co_3O_4 until the temperature reaches 300 °C, because the nucleation and grain growth of Co_3O_4 nanoparticles derived from the oxidation of Co ions could only happen when carbogels begin to

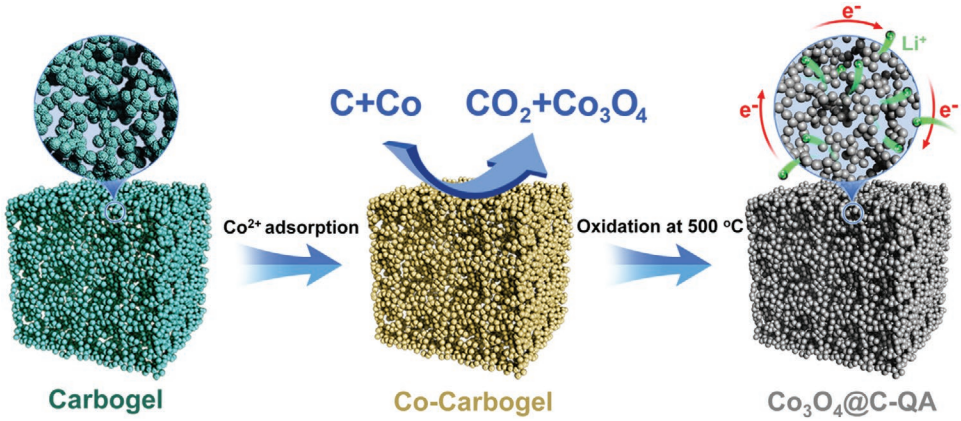

Figure 1. Schematic diagram of the preparation procedures of the Co_3O_4@carbon quasiaerogels (Co_3O_4@C-QA).

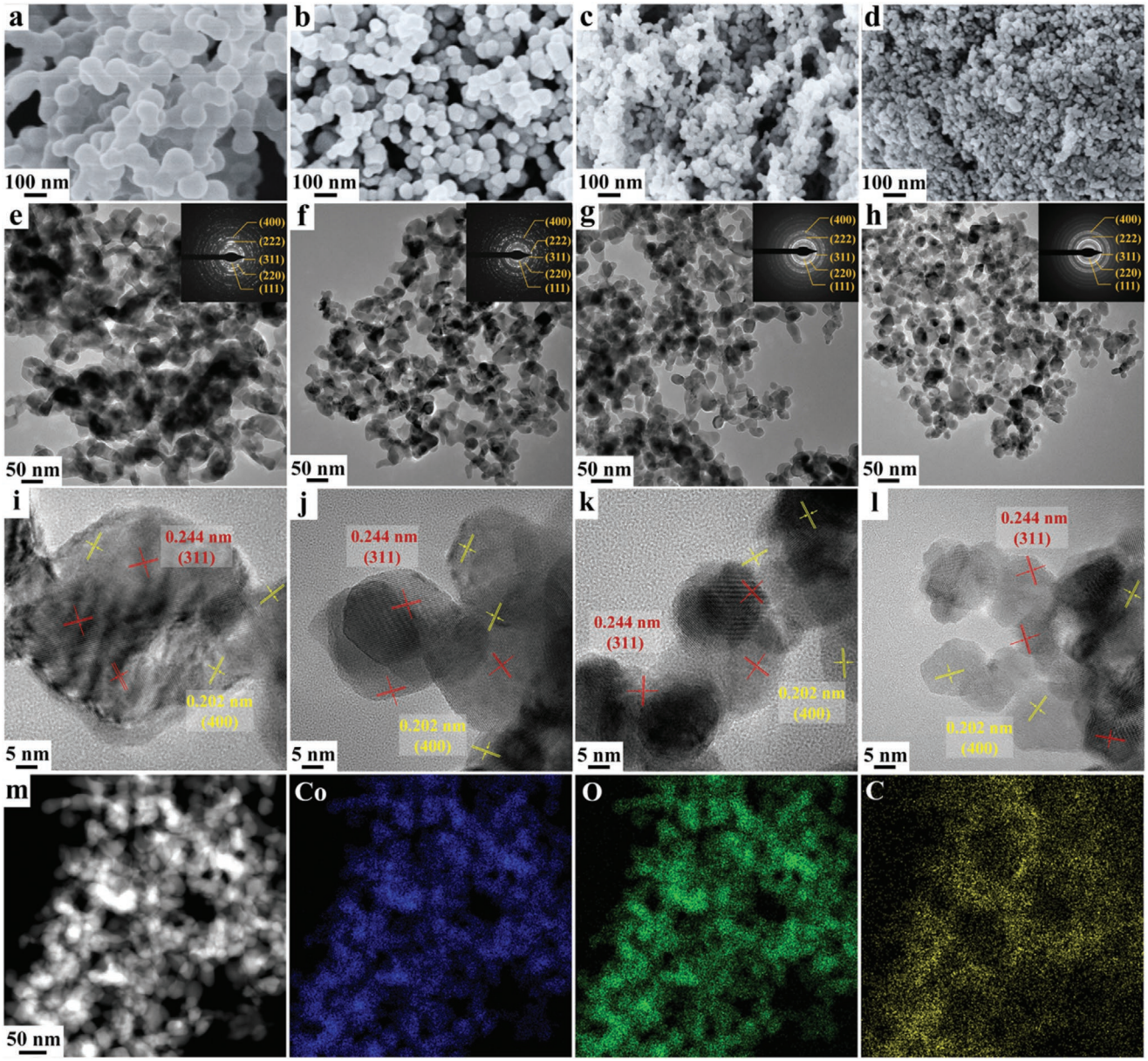

Figure 2. Morphology characterizations of various Co_3O_4@C-QA structures of 3D interconnected Co_3O_4 subunits with controllable diameters. FESEM images of a) Co_3O_4@C-QA-1, b) Co_3O_4@C-QA-2, c) Co_3O_4@C-QA-3, and d) Co_3O_4@C-QA-4. TEM images and corresponding SAED patterns of e) Co_3O_4@C-QA-1, f) Co_3O_4@C-QA-2, g) Co_3O_4@C-QA-3, and h) Co_3O_4@C-QA-4. HRTEM images of i) Co_3O_4@C-QA-1, j) Co_3O_4@C-QA-2, k) Co_3O_4@C-QA-3, and l) Co_3O_4@C-QA-4. m) HAADF-STEM image and EDX elemental mapping of Co, O, C within the Co_3O_4@C-QA-3 framework.

decompose as temperature is approaching 300 °C (Figure S6, Supporting Information).

FESEM images of the Co_3O_4@C-QA indicate that the diameter of the Co_3O_4 nanoparticle subunits among the Co_3O_4@C-QA is controlled, ranging from 15 to 85 nm (**Figure 2**a–d, Figure S7, Supporting Information). Due to the consumption of carbogel in the air, the particle size of the as-prepared Co_3O_4@C-QA is smaller than that of the subunits among the carbogel templates. Control sample of bulk Co_3O_4 obtained by directly oxidizing the cobalt (II) acetate tetrahydrate at 500 °C in air exhibits a morphology of irregular particles with severe aggregation (Figure S8, Supporting Information). Moreover, the large aggregations with uneven particle sizes of the Co_3O_4, obtained by oxidizing the cobalt (II) acetate tetrahydrate treated in an autoclave (Figure S9, Supporting Information), suggest that the carbogel template plays an essential role in achieving the 3D interconnected network of Co_3O_4@C-QA. Transmission electron microscopy (TEM) images further indicate that the Co_3O_4@C-QA consists of spherical nanoparticles with a narrow particle size distribution (Figure 2e–h), and these spherical nanoparticles interconnect with each other to form a 3D Co_3O_4 network with efficient ion transport pathways. The diameter of spherical Co_3O_4 nanoparticles can be adjusted to be 85, 38, 23, and 15 nm by merely employing the carbogel-1, carbogel-2,

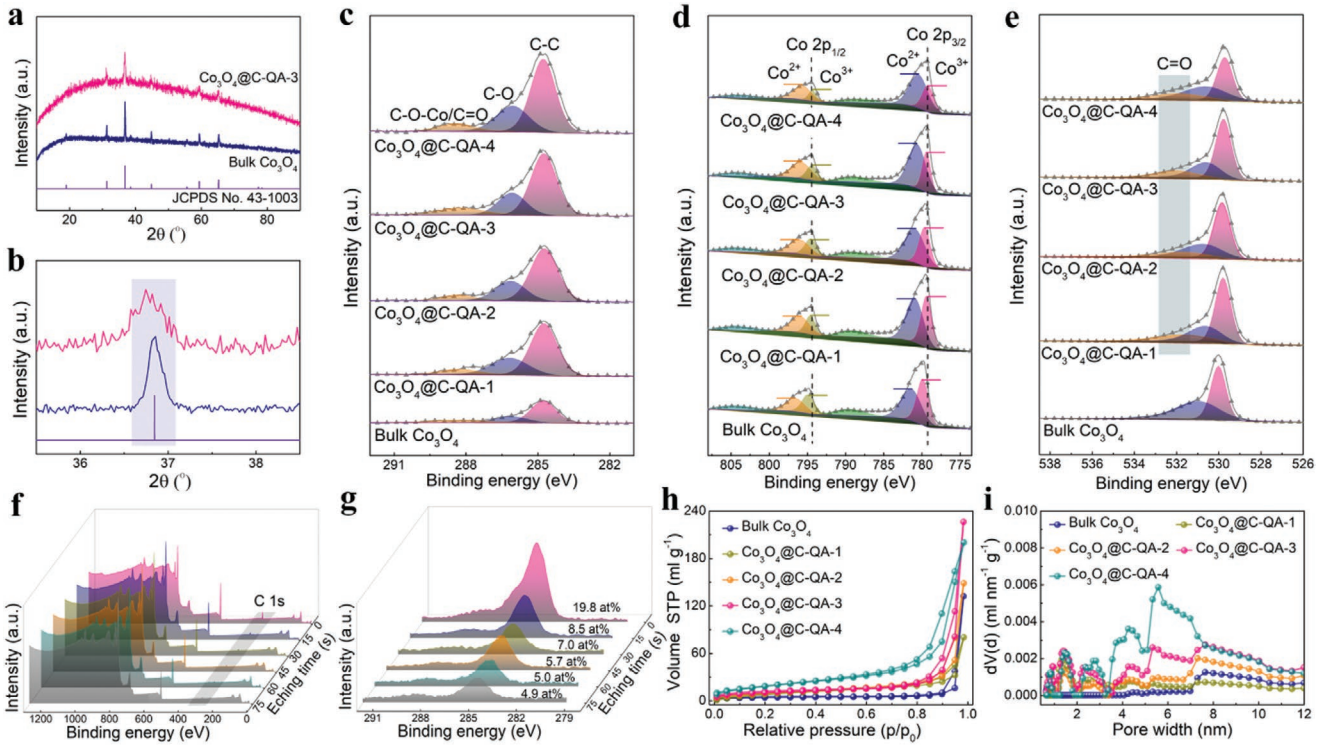

Figure 3. Composition and pore structure characterizations of the Co_3O_4@C-QA. Comparison of a) XRD patterns and b) selected (311) diffraction planes of bulk Co_3O_4 and Co_3O_4@C-QA-3. c) C 1s, d) Co 2p, e) O 1s XPS spectra of bulk Co_3O_4 and Co_3O_4@C-QA. XPS spectra of the Co_3O_4@C-QA-3 with argon ion etched for different time: f) Full spectra; g) C 1s spectra. h) Nitrogen sorption/desorption isotherms and i) pore size distributions of bulk Co_3O_4 and Co_3O_4@C-QA.

carbogel-3, and carbogel-4 templates, respectively. High-resolution TEM (HRTEM) images confirm that each Co_3O_4 nanoparticle among the Co_3O_4@C-QA shows a single-crystalline feature with lattice fringe spacing of 0.202 and 0.244 nm (Figure 2i–l), corresponding to (400) and (311) crystalline planes of spinel Co_3O_4, respectively.[6] Selected area electron diffraction (SAED) patterns further prove the spinel Co_3O_4 phase among the Co_3O_4@C-QA (inset of Figure 2e–h). High-angle annular dark-field scanning TEM (HAADF-STEM) image and corresponding elemental mappings demonstrate the co-existence of carbon species throughout the Co_3O_4@C-QA (Figure 2m).

The XRD patterns of Co_3O_4@C-QA and bulk Co_3O_4 are indexed to cubic spinel Co_3O_4 (JCPDS No. 43–1003, **Figure 3**a, Figure S10a, Supporting Information). Compared with bulk Co_3O_4, the Co_3O_4@C-QA-3 clearly shows the diffraction pattern ascribing to (311) crystalline plane shifting to small angular direction, suggesting the lattice parameter of Co_3O_4 phase among the Co_3O_4@C-QA-3 slightly increases due to the insertion of tetravalent carbon (Figure 3b).[40] According to the Debye-Scherrer equation, the average crystallite sizes among the Co_3O_4@C-QA-1, Co_3O_4@C-QA-2, Co_3O_4@C-QA-3, and Co_3O_4@C-QA-4 were calculated to be 76.4, 32.2, 26.3, and 16.7 nm, respectively, corresponding to the TEM results. The decreased particle sizes of the Co_3O_4@C-QA accompanied by increased half-peak widths (Figure S10b, Supporting Information), suggest that high crystallinity is deteriorated, especially for small-size Co_3O_4.[41] XPS spectra indicate the bonding configurations between Co_3O_4 hosts and doped carbon species. Figure S11a (Supporting Information) shows the full XPS spectra of Co_3O_4@C-QA and bulk Co_3O_4. The peaks of C 1s, O 1s and Co 2p are clearly observed. Three peaks at 284.8, 286.1, and 288.3 eV are deconvoluted from high-resolution C 1s spectra of the Co_3O_4@C-QA (Figure 3c), which are attributed to C=C, C—O, and C—O—Co/C=O, respectively.[41,42] On the contrary, the peak of C—O—Co/C=O in bulk Co_3O_4 is invisible, indicating that the doping of tetravalent carbon among the Co_3O_4@C-QA is closely related to carbogel templates. Note that atomic contents of C species in the Co_3O_4@C-QA-1, Co_3O_4@C-QA-2, Co_3O_4@C-QA-3, and Co_3O_4@C-QA-4 increase from 15.0 to 20.5 at%, and all these contents are much higher than that of bulk Co_3O_4 (6.7 at%) (Figure S11b, Supporting Information).

The high-resolution Co 2p spectra indicate that binding energy of Co_3O_4@C-QA at 794.3 eV (Co $2p_{1/2}$) and 779.3 eV (Co $2p_{3/2}$) shift to 795.9 and 779.9 eV (bulk Co_3O_4) (Figure 3d), demonstrating increased electronic density of Co among the Co_3O_4@C-QA.[41] Since more Co^{2+} ions are required to balance the charges, Co^{2+}/Co^{3+} ratio increases with higher tetravalent carbon doping content in Co_3O_4. Meanwhile, the high-resolution O 1s spectra show the peak at 532.3 eV corresponding to C=O, further proving the presence of carbon species among the Co_3O_4@C-QA (Figure 3e).[43] The depth-profiling XPS experiment of the Co_3O_4@C-QA-3 was carried out to investigate the carbon species distribution among the subunits of Co_3O_4@C-QA further. Notably, the atomic content of carbon species among the Co_3O_4@C-QA-3 significantly decreases from 19.8 to 8.5 at% after etching for 15 s while

only slight declines are observed during subsequent etching for 60 s (Figure 3f,g). This suggests that carbon species are enriched on the surface of Co_3O_4 nanoparticles among the Co_3O_4@C-QA-3. As a result, the Co_3O_4@C-QA exhibits a unique dual-channel aerogel structure, namely, electrically conductive carbon species are enriched on the surface of electrochemical active Co_3O_4 subunits. The thermogravimetric analysis (TGA) measurements of the Co_3O_4@C-QA were investigated to determine the exact contents of carbon species among the Co_3O_4@C-QA (Figure S12, Supporting Information). The TGA results indicate that there are ≈1.25, 1.47, 1.65, and 1.82 wt% of carbon species among the Co_3O_4@C-QA-1, Co_3O_4@C-QA-2, Co_3O_4@C-QA-3, and Co_3O_4@C-QA-4, respectively. Nitrogen adsorption-desorption isotherms were measured for the Co_3O_4@C-QA and bulk Co_3O_4 to determine their porosity and specific surface area (Figure 3h,i). Type IV characteristic curves with H1 hysteresis loop of the Co_3O_4@C-QA confirm the presence of mesopores.[44,45] The corresponding pore size distributions indicate relative abundant micro-/mesopores among the Co_3O_4@C-QA.[46–48] The surface areas of Co_3O_4@C-QA-1, Co_3O_4@C-QA-2, Co_3O_4@C-QA-3, and Co_3O_4@C-QA-4 are calculated as 17.4, 22.0, 30.9, and 45.9 $m^2\ g^{-1}$, respectively, much higher than that of bulk Co_3O_4 (9.1 $m^2\ g^{-1}$), which could facilitate an adequate exposure of electrochemically active sites.

During the combustion in air, the usual assumption is that infiltrated cobalt ions convert into Co_3O_4, while carbogel templates are consumed by reacting with O_2 to turn into CO_2.[49] Surprisingly, carbon species are observed to be enriched on the surface of as-obtained Co_3O_4 subunits among the Co_3O_4@C-QA. Ex-situ TEM observations of intermediates at different stages of self-embedded templating reaction indicate the formation mechanism for the Co_3O_4@C-QA. Four temperatures of 300, 400, 450, and 500 °C were used as the combustion temperature to monitor their morphological evolution from Co-carbogel to Co_3O_4@C-QA. **Figure 4**a indicates the formation mechanism of the Co_3O_4@C-QA. At the early stage, uniformly infiltrated cobalt ions within the Co-carbogels first undergo heterogeneous nucleation to form extremely small Co_3O_4 nanocrystals (Figure 4b), when the carbogel matrix begins to decompose. As the further reaction proceeds, the decomposition of carbogel will become more violent. According to the Ostwald ripening principle, larger particles possess lower surface energy. Thus, to minimize the total free energy, relatively smaller in-situ grown Co_3O_4 nanocrystals tend to be ablated and fuse into larger ones (Figure 4c).[50,51] Consequently, small Co_3O_4 nanocrystals continue to shrink while relatively large nanoparticles continue to grow (Figure 4d), during which the carbogel gradually decomposes into small organic molecules (such as hydrocarbons, C_xH_y). Part of the organic small molecule gas is combusted, but the other part is captured by in-situ grown Co_3O_4 nanoparticles and then carbonized into carbon on the surface of the Co_3O_4. As a result, the dual-channel aerogel structure of the Co_3O_4 nanoparticle network with a surface-enriched carbon network among the Co_3O_4@C-QA is obtained (Figure 4e).

Based on the proposed formation mechanism of the Co_3O_4@C-QA, various dual-channel TMO@C-QA with controllable particle sizes by employing carbogel-3 as the template has been prepared, demonstrating the versatility of the self-embedded templating strategy toward the general preparation of TMO@C-QA with unique 3D interconnected aerogel structure. The Fe_2O_3@C-QA, NiO@C-QA and Mn_3O_4@C-QA represent the TMO@C-QA using iron acetate, nickel acetate and manganese acetate as transition metal precursors, respectively, under other preparation conditions similar to the Co_3O_4@C-QA-3. The FTIR spectra of carbogel and M-carbogel confirm that Fe^{2+}, Ni^{2+} and Mn^{2+} ions are successfully infiltrated into the carbogels (Figure S13, Supporting Information). Upon combustion, the as-obtained Fe_2O_3@C-QA, NiO@C-QA and Mn_3O_4@C-QA all exhibit a 3D interconnected aerogel structure with uniform particle sizes (**Figure 5**a–c), similar to that of Co_3O_4@C-QA-3. HRTEM and SAED provide single-crystalline features and lattice fringe spacing of dual-channel

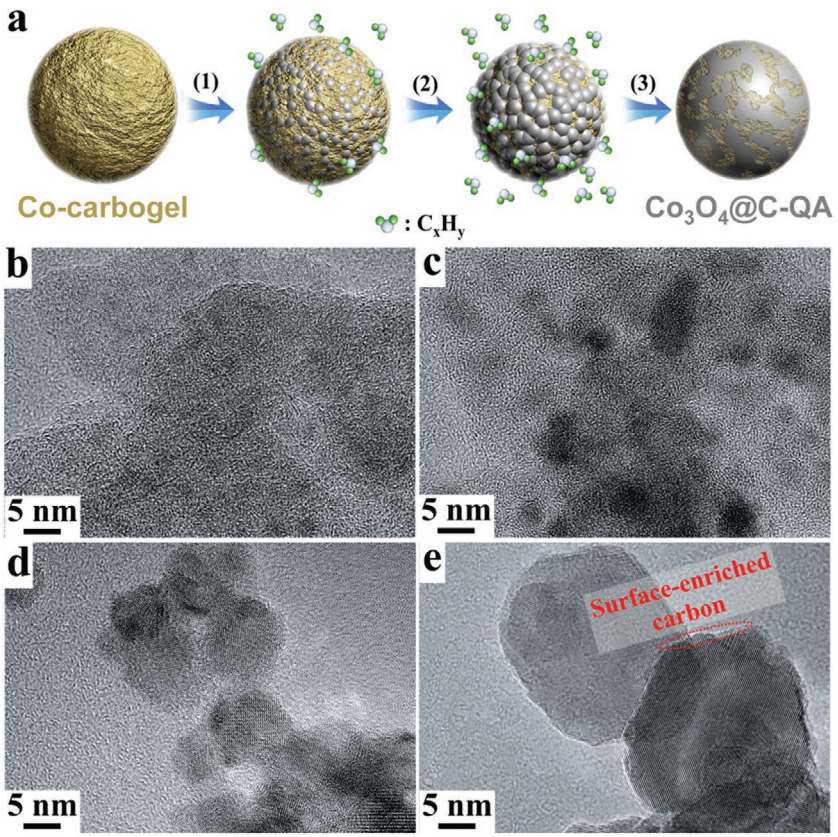

Figure 4. Formation mechanism of the Co_3O_4@C-QA in self-embedded templating strategy. a) Schematic illustration of the self-embedded Ostwald ripening templating processes: 1) formation of numerous extremely tiny Co_3O_4 nanocrystals as nucleation sites; 2) growth of large Co_3O_4 nanocrystals with the consumption of carbogel template; 3) formation of large-size and good-crystalline Co_3O_4 nanocrystals with surface-enriched carbon structures. b–e) Ex situ TEM images of the intermediates of Co-carbogels upon combustion.

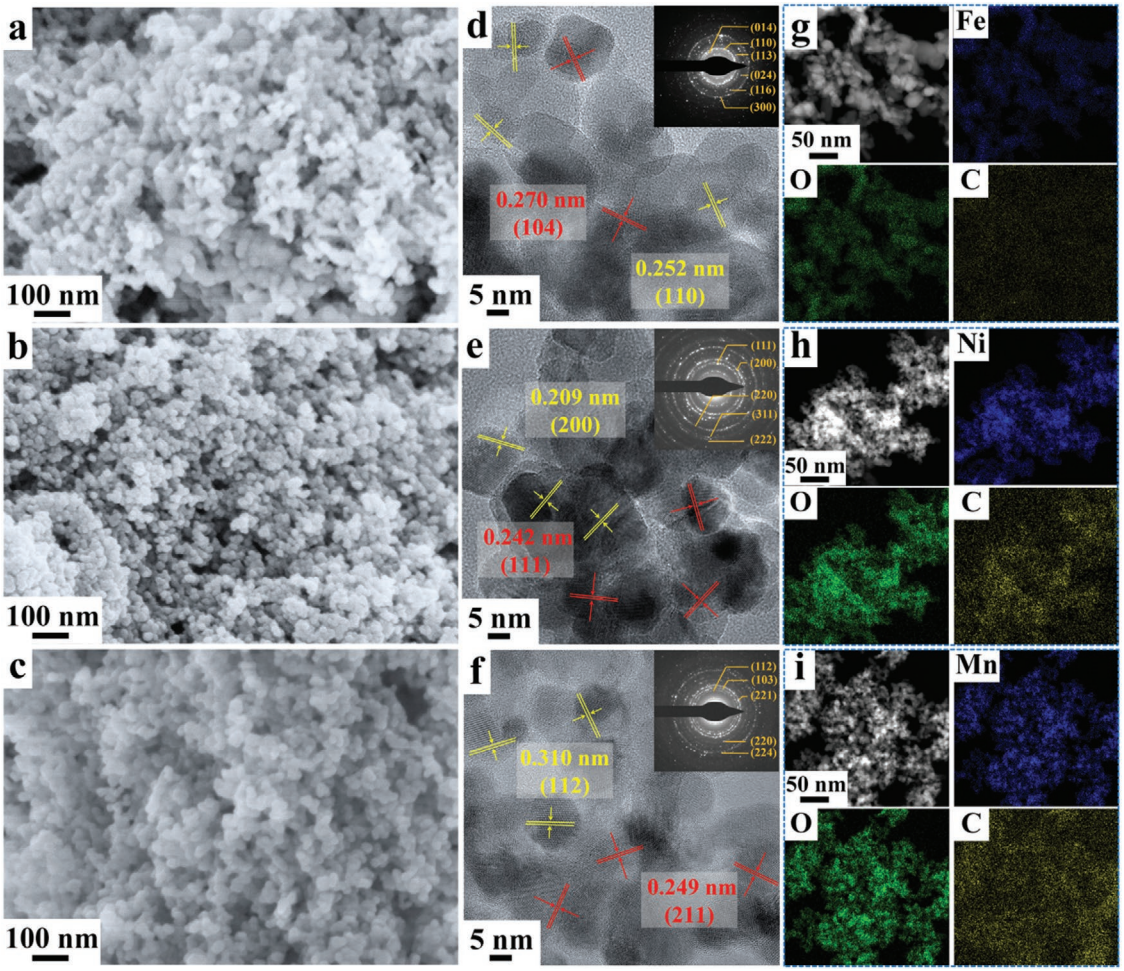

Figure 5. FESEM images of a) Fe_2O_3@C-QA, b) NiO@C-QA, and c) Mn_3O_4@C-QA. HRTEM images and corresponding SAED patterns of d) Fe_2O_3@C-QA, e) NiO@C-QA, and f) Mn_3O_4@C-QA. HAADF-STEM images and EDX elemental mapping of g) Fe_2O_3@C-QA, h) NiO@C-QA, and i) Mn_3O_4@C-QA.

TMO@C-QA (Figure 5d–f), which are consistent with XRD results (Figure S14, Supporting Information). HAADF-STEM images and corresponding elemental mappings reveal that carbon species are also uniformly incorporated within the TMO@C-QA (Figure 5g–i).

The TMO@C-QA with dual-channel aerogel structure exhibits high potentials for advanced electrochemical energy conversion. First, the spherical nanoparticle subunits among the TMO@C-QA typically show optimal thermodynamic stability compared with other geometries. Second, the 3D interconnected network of TMO@C-QA with extremely small TMO nanoparticles not only provides a large contact area between electrode and electrolytes, but also shortens ion transport channels. Third, the TMO@C-QA with a dual-channel aerogel structure will drastically reduce the electrical resistance between individual Co_3O_4 nanoparticles, thereby accelerating the kinetics of electrochemical reaction due to the reduced the overall resistance among electrode matrix. Finally, the 3D interconnected structure in dual-channel TMO@C-QA contributes to the prominent cycling stability by buffering internal stress in all directions during electrochemical process.

Bifunctional OER and HER electrocatalytic performance of the Co_3O_4@C-QA were investigated. **Figure 6**a manifests typical linear sweep voltammetry (LSV) curves of the Co_3O_4@C-QA, bulk Co_3O_4 and IrO_2 catalysts in 1 M KOH electrolyte. The Co_3O_4@C-QA-3 catalyst presents the most remarkable OER activity in comparison to other catalysts. The Co_3O_4@C-QA-3 catalyst requires a low overpotential of 370 mV to reach the current density of 10 mA cm^{-2} for the OER, which is 84, 63, 11, 16, and 5 mV lower than those of bulk Co_3O_4, Co_3O_4@C-QA-1, Co_3O_4@C-QA-2, Co_3O_4@C-QA-4, and IrO_2, respectively. The Co_3O_4@C-QA-3 catalyst presents the lowest OER Tafel slope (59.4 mV dec^{-1}) (Figure 6b), manifesting the fastest OER kinetics. Electrochemical impedance spectroscopy (EIS) was performed to investigate charge transport kinetics of Co_3O_4@C-QA catalysts. The Co_3O_4@C-QA catalysts (Figure S15, Supporting Information) possess low charge transfer resistance (R_{ct} = 7.0 ± 0.5 Ω) during OER process, which could accelerate the OER kinetics significantly.[52] To further investigate the intrinsic catalytic activities of Co_3O_4@C-QA and bulk Co_3O_4 catalysts, electrochemical surface areas (ECSAs) were calculated by measuring the double-layer capacitance of these catalysts (C_{dl}, Figure S16, Supporting Information).[53,54] Even though Co_3O_4@C-QA-4

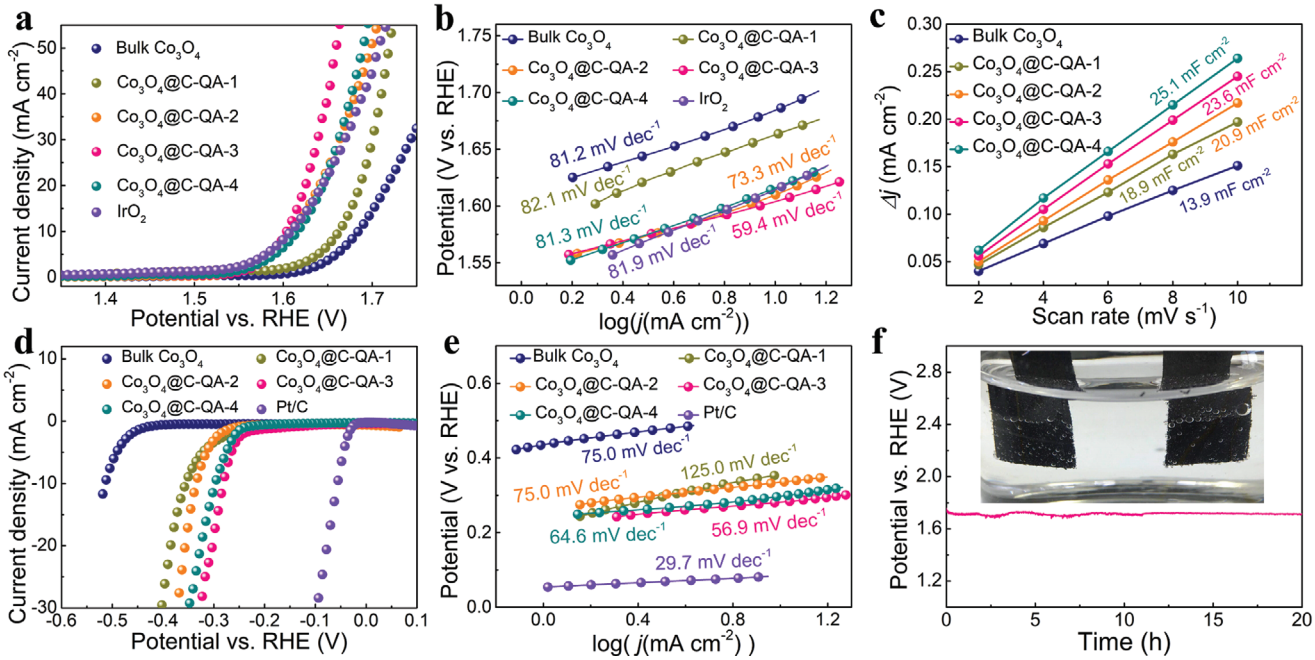

Figure 6. Bifunctional OER/HER performance of the Co_3O_4@C-QA. OER performance of Co_3O_4@C-QA, bulk Co_3O_4 and benchmark IrO_2: a) LSV curves at 5 mV s^{-1}; b) Tafel slopes; c) capacitive current as a function of scan rates for Co_3O_4@C-QA and bulk Co_3O_4. HER performance of Co_3O_4@C-QA, bulk Co_3O_4 and benchmark Pt/C: d) LSV curves at 5 mV s^{-1}; e) Tafel slopes. f) Chronoamperometric response of an electrolyzer using the Co_3O_4@C-QA-3 as the cathode and anode at 10 mA cm^{-2}. Inset of (f) showing H_2 (right) and O_2 (left) evolution.

catalyst possesses higher C_{dl} value than that of Co_3O_4@C-QA-3, the Co_3O_4@C-QA-3 catalyst exhibits higher catalytic activity (Figure 6c). This could be explained by the destruction of crystallinity, since the electrochemical activity of catalysts is significantly weakened as the crystallinity of TMO decreases.[55] The HER activities of Co_3O_4@C-QA, bulk Co_3O_4 and Pt/C catalysts were evaluated in 1 M KOH electrolyte. The LSV curves present that the Pt/C catalyst exhibits the lowest overpotential of 40 mV at the current density of 10 mA cm^{-2} for the HER. The Co_3O_4@C-QA catalyst shows a low overpotential of 280 mV for the HER, apparently smaller than that of bulk Co_3O_4 (514 mV), Co_3O_4@C-QA-1 (357 mV), Co_3O_4@C-QA-2 (336 mV), and Co_3O_4@C-QA-4 (298 mV) (Figure 6d). The fitted Tafel slope of the Co_3O_4@C-QA-3 catalyst (56.9 mV dec^{-1}) is the lowest value among the Co_3O_4@C-QA catalysts (Figure 6e). Moreover, the Co_3O_4@C-QA-3 catalysts prove its superior catalytic durability for both OER and HER, since there is only a slight deterioration in the electrochemical performance even after 100 h of cycling testing for the OER and HER (Figures S17 and S18, Supporting Information). Figures S19 and S20 (Supporting Information) display the FESEM images of the Co_3O_4@C-QA-3 catalysts after 100 h cycling of the OER and HER performance, respectively. The 3D interconnected network maintenance of the Co_3O_4@C-QA-3 during the long-term cycling process suggests the excellent structural stability of the Co_3O_4@C-QA-3 as a bifunctional catalyst. As a demonstration, an alkaline electrolyzer using Co_3O_4@C-QA-3 catalyst as both cathode and anode was built, manifesting an almost constant current density after operating at a required potential of 1.71 V to reach a current density of 10 mA cm^{-2} for 20 h cycling (Figure 6f). Table S1 (Supporting Information) summarizes the electrochemical activities of 3D structured bifunctional OER/HER electrocatalysts previously reported in the literatures, indicating that the Co_3O_4@C-QA catalyst is a promising bifunctional electrocatalyst among the state-of-the-art OER/HER bifunctional electrocatalysts.

Electrochemical performance of Co_3O_4@C-QA and bulk Co_3O_4 as LIB anode was evaluated by cyclic voltammetry (CV) and galvanostatic charge/discharge (GCD) measurements over the potential window of 0.01–3.00 V. The initial three CV curves of the Co_3O_4@C-QA electrodes at 0.1 mV s^{-1} are illustrated in Figure S21 (Supporting Information). In the first cycle, an irreversible peak appears at 0.78 V, which is associated with the formation of a solid electrolyte interface (SEI) film.[56,57] In the subsequent two cycles, two reversible redox peaks at 1.10 and 2.05 V are contributed to the reduction of Co^{2+} to metallic Co and the oxidation of metallic Co to CoO,[58] respectively. The typical GCD profiles for the first, second, and fifth cycles are presented in **Figure 7**a. An apparent long plateau is observed around at 0.7–0.9 V in the first discharge curve. The plateau slightly shifts upward to 0.8–1.3 V in the second discharge curve. The initial Coulombic efficiency of 76.8%, and the irreversible capacity loss is mainly attributed to the formation of SEI film. The comparison of the electrochemical performance of the Co_3O_4@C-QA with other cobalt oxide-based anode materials clearly suggests that the Co_3O_4@C-QA is an ideal anode material for LIBs, which are better than most cobalt oxide-based anode materials reported in other literatures (Table S2, Supporting Information).

Excellent rate performance and cyclic performance are critical for the practical applications of anode materials for LIB. The Co_3O_4@C-QA electrodes deliver a much higher and more

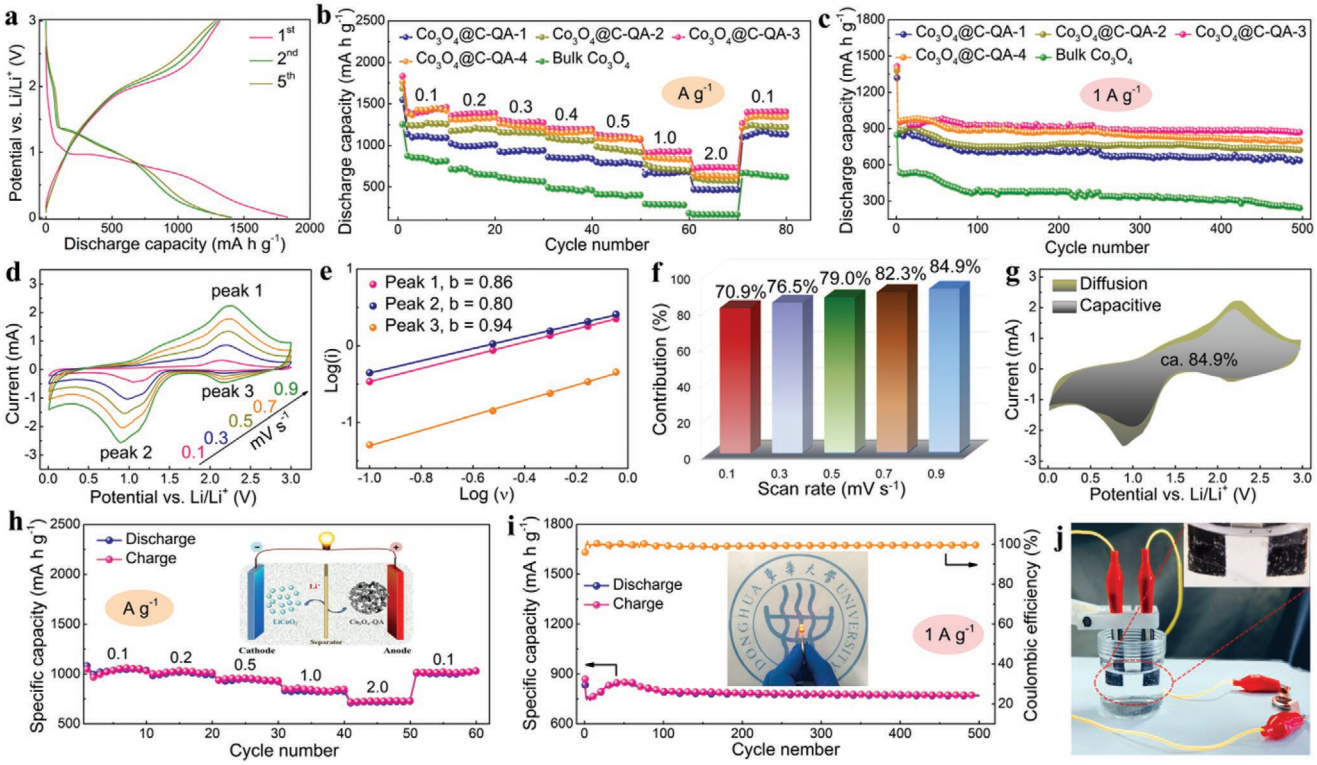

Figure 7. Fully battery-powered water electrolysis performance of the Co_3O_4@C-QA: a) GCD curves of the Co_3O_4@C-QA-3 at 0.1 A g^{-1}. b) Rate performance of the Co_3O_4@C-QA and bulk Co_3O_4 from 0.1 to 2 A g^{-1}. c) Cycling performance of the Co_3O_4@C-QA and bulk Co_3O_4 at 1 A g^{-1}. Kinetic investigation of the Co_3O_4@C-QA-3: d) CV curves at different scan rates; e) corresponding log(peak current) versus log(scan rate) plots at different redox states; f) chart shows the contribution of capacitive behavior at different scan rates; g) CV curves of capacitive and diffusion contribution at 0.9 mV s^{-1}. Electrochemical performance of the Co_3O_4@C-QA-3//$LiCoO_2$ full cell: h) rate performance at different current density, inset of (h) showing the assembly of LIB full cell; i) cycling performance of the full cell at 1 A g^{-1}, inset of (i) showing an LED light powered by two series-connected full cells; j) photograph showing an electrolyzer powered by two series-connected full cells, inset of (j) showing H_2 (right) and O_2 (left) evolution.

stable Li-storage capacity compared with that of bulk Co_3O_4, when operated at various current density of 0.1–2.0 A g^{-1} (Figure 7b). Remarkably, the Co_3O_4@C-QA-3 electrode exhibits extremely high reversible capacity of 1405, 1368, 1265, 1195, 1102, 918, and 730 mA h g^{-1}, at the discharge current density of 0.1, 0.2, 0.3, 0.4, 0.5, 1.0, and 2.0 A g^{-1}, respectively. The specific discharge capacity of Co_3O_4@C-QA-3 electrode rises to 1398 mA h g^{-1} when the current density restores from 2.0 to 0.1 A g^{-1}, which is almost equal to its initial discharge capacity. Furthermore, the Co_3O_4@C-QA electrodes exhibit outstanding long-term Li-storage stability at 1.0 A g^{-1} (Figure 7c). All the Co_3O_4@C-QA electrodes present a similar activation tendency with slight fluctuations of specific capacity over the previous 70 cycles, due to the growth of pseudocapacitive film on the electrode surface. Eventually, the specific capacity of Co_3O_4@C-QA-3 electrode maintains at 880 mA h g^{-1}, overmatching the Co_3O_4@C-QA-1 (636 mA h g^{-1}), Co_3O_4@C-QA-2 (718 mA h g^{-1}) and Co_3O_4@C-QA-4 (807 mA h g^{-1}). In contrast, bulk Co_3O_4 electrode suffers a severe fading with only 234 mA h g^{-1} after 500 charge/discharge cycles. The remarkable capability and cycling stability of Co_3O_4@C-QA electrodes benefit from largely improved electrical conductivity,[59] evidenced by EIS results in Figure S22 (Supporting Information). The Co_3O_4@C-QA electrodes show smaller diameters of semicircles than that of bulk Co_3O_4 in the high-frequency area. The low R_{ct} values of Co_3O_4@C-QA electrodes are mainly attributed to the formation of a 3D interconnected aerogel structure with surface-enriched carbon species among the Co_3O_4@C-QA electrode.

CV curves of Co_3O_4@C-QA-3 electrode at different scan rates (0.1, 0.3, 0.5, 0.7, and 0.9 mV s^{-1}) were displayed to estimate its kinetic properties (Figure 7d), suggesting negligible polarization during successive charge/discharge processes. The faradic and nonfaradic (pseudocapacitive) proportions contributing Li-storage at different scan rates were assessed by equations as follows.[60–62] In Equation (1), i represents the (peak) current and v represents the scan rate. The value of b in Equation (2) is calculated by the slope of log(i)–log(v). During the electrochemical reaction, if b is close to 0.5, ion diffusion is the dominant contribution; if b is close to 1.0, pseudocapacitive contribution plays a significant role. In Equation (3), $i(V)$ denotes the current at a specific potential, k_1v and $k_2v^{0.5}$ represent the capacitive and diffusion-controlled contribution, respectively. The calculated b values of peaks 1–3 are 0.86, 0.80, and 0.94 (Figure 7e), respectively, clearly indicating that capacitive behavior dominate the electrochemical reaction of Co_3O_4@C-QA-3 electrode. Figure 7f shows the capacitive contribution of Co_3O_4@C-QA-3 electrode at various scan rates. The capacitive contribution of Co_3O_4@C-QA-3 electrode increases with increased scan rates. Based on the calculation, the proportion of capacitive behavior among the Co_3O_4@C-QA-3 electrode at 0.9 mV s^{-1} could reach

84.9% (Figure 7g). The great capacitive contribution of the Co_3O_4@C-QA-3 electrode stems from the following reasons: 1) 3D interconnected aerogel structure of extremely tiny Co_3O_4 nanocrystals provides a large accessible surface area with more accommodated Li-ions and improved surface pseudocapacitance; 2) surface-enriched carbon within the Co_3O_4@C-QA acts as electron-accepting pairs enhancing the interfacial double-layer capacitance:

$$i = av^b \tag{1}$$

$$\log(i) = b \times \log(v) + \log(a) \tag{2}$$

$$i(V) = kv + kv^{0.5} \tag{3}$$

The Co_3O_4@C-QA-3 electrode is further assessed as an anode in LIB full cell by using commercial $LiCoO_2$ as the cathode, and the as-assembled full cell is denoted as Co_3O_4@C-QA-3//$LiCoO_2$. Inset of Figure 7h shows a schematic illustration of the assembly of Co_3O_4@C-QA-3//$LiCoO_2$ battery. The LIB full cell was assembled according to the mass ratio of the anode to the cathode at 1:9 to achieve the matching of cathode and anode capacity. The electrochemical performance of the Co_3O_4@C-QA-3//$LiCoO_2$ battery was investigated by GCD measurements over the voltage range of 1.0–4.0 V at a current density of 1.0 A g^{-1}. The clear charge/discharge voltage plateau indicates the Co_3O_4@C-QA-3 anode stores and releases Li^+ successfully from commercial $LiCoO_2$ cathode (Figure S23, Supporting Information). Figure 7h shows the rate performance of the Co_3O_4@C-QA-3//$LiCoO_2$ battery, and extremely high capacity of 1032, 1006, 937, 825, 718 mA h g^{-1} are achieved based on anode material at the current density of 0.1, 0.2, 0.5, 1.0, 2.0 A g^{-1}, respectively. Figure 7i demonstrates superior cycling performance of the Co_3O_4@C-QA-3//$LiCoO_2$ battery. The specific capacity could still maintain at 770 mA h g^{-1} with Coulombic efficiency up to 99.8%, even after operating 500 charge/discharge cycles at 1 A g^{-1}.

The high specific capacity, long-term stability and outstanding rate performance of the Co_3O_4@C-QA anode are interpreted by its unique 3D interconnected aerogel structure. First, the Co_3O_4@C-QA with a 3D interconnected aerogel structure not only facilitates the lithiation/delithiation process with a short ion diffusion pathway, but also alleviates the volume change by releasing localized stress. Besides, the Co_3O_4@C-QA with a 3D interconnected aerogel structure realizes the formation of a 3D conductive network with promoted charge transfer due to surface-enriched carbon species. Moreover, more Co^{2+} species formation due to tetravalent carbon insertion into Co_3O_4 among the Co_3O_4@C-QA enhances the electrochemical activity significantly, since Co^{2+} shows faster Co^{2+}/Co^0 redox reaction and stronger electronegativity than that of neat Co_3O_4.[40]

Red light-emitting diodes (LEDs) can be easily lighted up, verifying practical applications of the Co_3O_4@C-QA-3//$LiCoO_2$ battery (inset of Figure 7i). The Co_3O_4@C-QA-3//$LiCoO_2$ battery is further employed for battery-powered water electrolysis. An alkaline electrolyzer with Co_3O_4@C-QA-3 loaded cathode and anode promotes the evolution of H_2 and O_2, respectively, which is powered by two series-connected Co_3O_4@C-QA-3//$LiCoO_2$ batteries. A large number of H_2 and O_2 bubbles are generated on the cathode and anode (Figure 7j and Movie S1, Supporting Information). The proof-of-concept battery-powered water electrolysis system shows great potentials of TMO@C-QA for multifunctional energy conversion applications.

3. Conclusion

In summary, the TMO@C-QA possessing a dual-channel aerogel structure of electrochemically active 3D interconnected TMO nanoparticles with surface-enriched carbon species was fabricated. The 3D interconnected aerogel structure formation of TMO@C-QA, among which electrochemical active TMO nanoparticles are surface-enriched with electrically conductive carbon species, is ascribed to self-embedded Ostwald ripening templating processes. The self-embedded templating strategy is a general method to prepare a variety of dual-channel TMO@C-QA, including the Co_3O_4@C-QA, Fe_2O_3@C-QA, NiO@C-QA, and Mn_3O_4@C-QA. Due to its unique structural features, the as-obtained Co_3O_4@C-QA shows excellent bifunctional electrocatalytic performance toward the OER (overpotential of 370 mV at 10 mA cm^{-2}) and HER (overpotential of 280 mV at 10 mA cm^{-2}), as well as superior lithium storage performance with high specific capacity (1405 mA h g^{-1} at 0.1 A g^{-1}) and outstanding cycle performance (500 cycles at 1 A g^{-1} without significant decay). As a proof-of-concept, the Co_3O_4@C-QA-3 is further assessed as the anode material in LIB full cell, delivering a high specific capacity of 770 mA h g^{-1} at 1.0 A g^{-1} with a Coulombic efficiency of 99.8%. Specifically, two series-connected LIB full cells successfully drive a full water electrolysis system, where the Co_3O_4@C-QA is employed as both anode and cathode for overall water splitting. This study, therefore, demonstrates that the self-embedded templating fabrication of a quasiaerogel interconnecting architecture enables the resulting TMO materials with high electrical conductivity, efficient ion transport and excellent electrochemical activity. The emerging dual-channel TMO-based quasiaerogels might pave the way for the development of next-generation high-performance LIBs and water splitting system with great potential to promote the practical applications in integrated energy conversion/storage systems.

4. Experimental Section

Preparation of Carbogel-X: Carbogels were prepared by hydrothermal carbonization using glucose and borax as the precursor and structure-directing agent, respectively. 25, 100, 250, and 600 mg of borax were dissolved in 15 mL of water with 6 g of glucose, respectively, transferred to Teflon-lined autoclaves, and heated at 180 °C for 8 h. The as-obtained hydrogel samples were extracted with water and ethanol to remove any impurities, and then freeze-dried to give light brown carbogels. The carbogels prepared at different sugar/borax ratios were denoted as carbogel-*X*, where *X* = 1, 2, 3, 4, corresponding to the borax amount of 25, 100, 250, and 600 mg, respectively.

Preparation of TMO-QA: Taking the preparation of Co_3O_4-QA as an example, 2.0 mmol of cobalt (II) acetate tetrahydrate was dissolved into 60 mL of ethylene glycol under stirring. Then, 500 mg of carbogel-*X* powder was dispersed into the above solution by sonication. The mixed dispersion was transferred to a Teflon-lined autoclave, heated at 120 °C for 12 h, and then heated at 170 °C for another 2 h. Upon cooling, the

precipitate was collected, and washed with water and ethanol several times. The as-obtained samples were labeled as Co-carbogel-*X*, where $X = 1, 2, 3, 4$, corresponding to the use of precursors of carbogel-1, carbogel-2, carbogel-3, and carbogel-4, respectively. The Co_3O_4-QA-*X* was obtained by oxidizing the as-obtained Co-carbogel-*X* samples in the air at 500 °C for 4 h, starting from room temperature (25 °C), with a heating rate of 3 °C min^{-1}. Other TMO-QAs (i.e., Fe_2O_3-QA, NiO-QA, and Mn_3O_4-QA) were prepared with a similar preparation process to that of the Co_3O_4-QA-3, except for the use of different transition metal acetate precursors.

Preparation of Bulk Co_3O_4: Bulk Co_3O_4 was obtained by oxidizing pulverized cobalt (II) acetate tetrahydrate in the air at 500 °C for 4 h, starting from room temperature (25 °C), with a heating rate of 3 °C min^{-1}.

Supporting Information

Supporting Information is available from the Wiley Online Library or from the author.

Acknowledgements

The authors are grateful for the financial support from the National Natural Science Foundation of China (51773035, 51433001), the Shanghai Rising-Star Program (18QA1400200), the Natural Science Foundation of Shanghai (17ZR1439900), the Program of Shanghai Academic Research Leader (17XD1400100), and the Shanghai Scientific and Technological Innovation Project (18JC1410600).

Conflict of Interest

The authors declare no conflict of interest.

Keywords

dual-channel heterostructures, quasiaerogels, self-embedded templating, transition-metal oxides, water electrolysis

Received: January 2, 2020
Published online: February 19, 2020

[1] A. A. AbdelHamid, Y. Yu, J. Yang, J. Y. Ying, *Adv. Mater.* **2017**, *29*, 1701427.
[2] L. Han, S. Dong, E. Wang, *Adv. Mater.* **2016**, *28*, 9266.
[3] Y. Zhao, X. F. Li, B. Yan, D. B. Xiong, D. J. Li, S. Lawes, X. L. Sun, *Adv. Energy Mater.* **2016**, *6*, 1502175.
[4] X. Zhang, J. Liu, Z. Zhang, S. Wu, Z. Tang, B. Guo, L. Zhang, *ACS Appl. Mater. Interfaces* **2018**, *10*, 23485.
[5] Y. P. Zhu, T. Y. Ma, M. Jaroniec, S. Z. Qiao, *Angew. Chem., Int. Ed.* **2017**, *56*, 1324.
[6] G. Huang, S. Xu, S. Lu, L. Li, H. Sun, *ACS Appl. Mater. Interfaces* **2014**, *6*, 7236.
[7] B. Q. Liu, Q. Zhang, Z. S. Jin, L. Y. Zhang, L. Li, Z. G. Gao, C. G. Wang, H. M. Xie, Z. M. Su, *Adv. Energy Mater.* **2018**, *8*, 1702347.
[8] K. X. Wang, X. H. Li, J. S. Chen, *Adv. Mater.* **2015**, *27*, 527.
[9] Y. Zhao, L. P. Wang, M. T. Sougrati, Z. X. Feng, Y. Leconte, A. Fisher, M. Srinivasan, Z. C. Xu, *Adv. Energy Mater.* **2017**, *7*, 1601424.
[10] M. Ciszewski, G. Benke, K. Leszczyńska-Sejda, *Compos. Commun.* **2018**, *8*, 42.
[11] S. Zhu, J. J. Li, X. Y. Deng, C. N. He, E. Z. Liu, F. He, C. S. Shi, N. Q. Zhao, *Adv. Funct. Mater.* **2017**, *27*, 1605017.
[12] Y.-G. Guo, J.-S. Hu, L.-J. Wan, *Adv. Mater.* **2008**, *20*, 2878.
[13] L. M. Zhou, K. Zhang, Z. Hu, Z. L. Tao, L. Q. Mai, Y. M. Kang, S. L. Chou, J. Chen, *Adv. Energy Mater.* **2018**, *8*, 1701415.
[14] J. Li, Y. Wang, T. Zhou, H. Zhang, X. Sun, J. Tang, L. Zhang, A. M. Al-Enizi, Z. Yang, G. Zheng, *J. Am. Chem. Soc.* **2015**, *137*, 14305.
[15] M. Li, H. Du, L. Kuai, K. Huang, Y. Xia, B. Geng, *Angew. Chem., Int. Ed.* **2017**, *56*, 12649.
[16] M. Zheng, H. Tang, L. Li, Q. Hu, L. Zhang, H. Xue, H. Pang, *Adv. Sci.* **2018**, *5*, 1700592.
[17] Y. Guo, T. Park, J. W. Yi, J. Henzie, J. Kim, Z. Wang, B. Jiang, Y. Bando, Y. Sugahara, J. Tang, Y. Yamauchi, *Adv. Mater.* **2019**, *31*, 1807134.
[18] C. Feng, J. Zhang, Y. He, C. Zhong, W. Hu, L. Liu, Y. Deng, *ACS Nano* **2015**, *9*, 1730.
[19] M. Niederberger, *Adv. Funct. Mater.* **2017**, *27*, 1703647.
[20] I. Vamvasakis, K. S. Subrahmanyam, M. G. Kanatzidis, G. S. Armatas, *ACS Nano* **2015**, *9*, 4419.
[21] E. Barrios, D. Fox, Y. Y. Li Sip, R. Catarata, J. E. Calderon, N. Azim, S. Afrin, Z. Zhang, L. Zhai, *Polymers* **2019**, *11*, 726.
[22] W. Cheng, F. Rechberger, M. Niederberger, *ACS Nano* **2016**, *10*, 2467.
[23] L. Huber, S. Zhao, W. J. Malfait, S. Vares, M. M. Koebel, *Angew. Chem., Int. Ed.* **2017**, *56*, 4753.
[24] J. Wang, X. Zhang, *ACS Nano* **2015**, *9*, 11389.
[25] S. S. Kistler, *Nature* **1931**, *127*, 741.
[26] B. Cai, A. Eychmuller, *Adv. Mater.* **2019**, *31*, 1804881.
[27] H. D. Gesser, P. C. Goswami, *Chem. Rev.* **1989**, *89*, 765.
[28] N. Leventis, *Acc. Chem. Res.* **2007**, *40*, 874.
[29] S. Mahadik-Khanolkar, S. Donthula, C. Sotiriou-Leventis, N. Leventis, *Chem. Mater.* **2014**, *26*, 1303.
[30] A. Benad, F. Jürries, B. Vetter, B. Klemmed, R. Hübner, C. Leyens, A. Eychmüller, *Chem. Mater.* **2017**, *30*, 145.
[31] B. X. Liu, X. C. Liu, X. F. Zhao, H. L. Fan, J. Zhang, X. B. Yi, M. Gao, L. Y. Zhu, X. Q. Wang, *Chem. Phys. Lett.* **2019**, *715*, 109.
[32] W. Liu, A. K. Herrmann, N. C. Bigall, P. Rodriguez, D. Wen, M. Oezaslan, T. J. Schmidt, N. Gaponik, A. Eychmuller, *Acc. Chem. Res.* **2015**, *48*, 154.
[33] G. Q. Zu, J. Shen, L. P. Zou, W. Q. Wang, Y. Lian, Z. H. Zhang, A. Du, *Chem. Mater.* **2013**, *25*, 4757.
[34] T. Y. Wei, C. H. Chen, H. C. Chien, S. Y. Lu, C. C. Hu, *Adv. Mater.* **2010**, *22*, 347.
[35] C. N. Sisk, L. J. Hope-Weeks, *J. Mater. Chem.* **2008**, *18*, 2607.
[36] T. Y. Wei, C. H. Chen, K. H. Chang, S. Y. Lu, C. C. Hu, *Chem. Mater.* **2009**, *21*, 3228.
[37] N. Husing, U. Schubert, *Angew. Chem., Int. Ed.* **1998**, *37*, 22.
[38] T.-P. Fellinger, R. J. White, M.-M. Titirici, M. Antonietti, *Adv. Funct. Mater.* **2012**, *22*, 3254.
[39] S. A. Rub Pakkath, S. S. Chetty, P. Selvarasu, A. Vadivel Murugan, Y. Kumar, L. Periyasamy, M. Santhakumar, S. R. Sadras, K. Santhakumar, *ACS Biomater. Sci. Eng.* **2018**, *4*, 2582.
[40] C. Yan, Y. Zhu, Y. Li, Z. Fang, L. Peng, X. Zhou, G. Chen, G. Yu, *Adv. Funct. Mater.* **2018**, *28*, 1705951.
[41] C. Yan, G. Chen, X. Zhou, J. Sun, C. Lv, *Adv. Funct. Mater.* **2016**, *26*, 1428.
[42] C. Dong, X. Yuan, X. Wang, X. Liu, W. Dong, R. Wang, Y. Duan, F. Huang, *J. Mater. Chem. A* **2016**, *4*, 11292.
[43] Z.-J. Jiang, S. Cheng, H. Rong, Z. Jiang, J. Huang, *J. Mater. Chem. A* **2017**, *5*, 23641.
[44] C. Zhang, M. Antonietti, T. P. Fellinger, *Adv. Funct. Mater.* **2014**, *24*, 7655.
[45] N. Wang, H. Tian, S.-Y. Zhu, D.-Y. Yan, Y.-Y. Mai, *Chin. J. Polym. Sci.* **2017**, *36*, 266.

[46] P. Ge, H. Hou, S. Li, L. Yang, X. Ji, *Adv. Funct. Mater.* **2018**, *28*, 1801765.
[47] J. Wang, H. Tang, L. Zhang, H. Ren, R. Yu, Q. Jin, J. Qi, D. Mao, M. Yang, Y. Wang, P. Liu, Y. Zhang, Y. Wen, L. Gu, G. Ma, Z. Su, Z. Tang, H. Zhao, D. Wang, *Nat. Energy* **2016**, *1*, 16050.
[48] Y. Wang, L. Yu, X. W. Lou, *Angew. Chem., Int. Ed.* **2016**, *55*, 7423.
[49] J. Parvole, I. Chaduc, K. Ako, O. Spalla, A. Thill, S. Ravaine, E. Duguet, M. Lansalot, E. Bourgeat-Lami, *Macromolecules* **2012**, *45*, 7009.
[50] T. Jiang, F. Bu, X. Feng, I. Shakir, G. Hao, Y. Xu, *ACS Nano* **2017**, *11*, 5140.
[51] J. Xie, X. Zhang, H. Zhang, J. Zhang, S. Li, R. Wang, B. Pan, Y. Xie, *Adv. Mater.* **2017**, *29*, 1604765.
[52] Y. Guo, J. Tang, H. Qian, Z. Wang, Y. Yamauchi, *Chem. Mater.* **2017**, *29*, 5566.
[53] Z. Q. Xue, Y. L. Li, Y. W. Zhang, W. Geng, B. M. Jia, J. Tang, S. X. Bao, H. P. Wang, Y. A. Fan, Z. W. Wei, Z. S. Zhang, Z. F. Ke, G. Q. Li, C. Y. Su, *Adv. Energy Mater.* **2018**, *8*, 1801564.
[54] Y. Guo, J. Tang, Z. Wang, Y.-M. Kang, Y. Bando, Y. Yamauchi, *Nano Energy* **2018**, *47*, 494.
[55] S. A. Pervez, D. Kim, U. Farooq, A. Yaqub, J. H. Choi, Y. J. Lee, C. H. Doh, *ACS Appl. Mater. Interfaces* **2014**, *6*, 11219.
[56] L. L. Luo, J. S. Wu, J. M. Xu, V. P. Dravid, *ACS Nano* **2014**, *8*, 11560.
[57] Q. M. Su, J. Zhang, Y. S. Wu, G. H. Du, *Nano Energy* **2014**, *9*, 264.
[58] Y. H. Dou, J. T. Xu, B. Y. Ruan, Q. N. Liu, Y. D. Pan, Z. Q. Sun, S. X. Dou, *Adv. Energy Mater.* **2016**, *6*, 1501835.
[59] Y. Yan, Z. Ma, H. Lin, K. Rui, Q. Zhang, Q. Wang, M. Du, D. Li, Y. Zhang, J. Zhu, W. Huang, *Compos. Commun.* **2019**, *13*, 97.
[60] B.-H. Hou, Y.-Y. Wang, D.-S. Liu, Z.-Y. Gu, X. Feng, H. Fan, T. Zhang, C. Lü, X.-L. Wu, *Adv. Funct. Mater.* **2018**, *28*, 1805444.
[61] Q. Tang, Y. Cui, J. Wu, D. Qu, A. P. Baker, Y. Ma, X. Song, Y. Liu, *Nano Energy* **2017**, *41*, 377.
[62] L. Shi, D. Li, P. Yao, J. Yu, C. Li, B. Yang, C. Zhu, J. Xu, *Small* **2018**, *14*, 1802716.